

## Crack-reduced laser powder bed fused oxide ceramic parts by in-situ synthesis of negative thermal expansion phases

Stefan Pfeiffer<sup>1,2\*</sup>, Kevin Florio<sup>3</sup>, Malgorzata Makowska<sup>4</sup>, Christos G. Aneziris<sup>2</sup>, Helena Van Swygenhoven<sup>4</sup>, Konrad Wegener<sup>3</sup>, Thomas Graule<sup>1,2</sup>

- 1) Laboratory for High Performance Ceramics, Empa – Swiss Federal Laboratories for Materials Science and Technology, Überlandstrasse 129, 8600 Dübendorf, Switzerland
- 2) Institute of Ceramic, Glass and Construction Materials, TU Bergakademie Freiberg, Agricolastraße 17, 09599 Freiberg, Germany
- 3) Institute of Machine Tools and Manufacturing, ETH Zürich, Leonhardstrasse 21, 8092 Zurich, Switzerland
- 4) Photon Science Division, Paul Scherrer Institut, 5232 Villigen PSI, Switzerland

**E-Mail: stefan.pfeiffer@empa.ch**

**Keywords:** laser powder bed fusion, selective laser melting, aluminum oxide, zirconium tungstate, aluminum tungstate

### Abstract

Both in industry and research, laser powder bed fusion is increasingly adopted for applications commonly involving metals and polymers. However, the application to other materials, specifically oxide ceramics, faces challenges for industrial implementations due to its unique properties, such as low thermal shock resistance, high brittleness and a low light absorptance level in the near-infrared range. This study provides a solution to increase powder absorptance at a wavelength of 1070 nm while also reducing cracking during laser processing of oxide ceramic parts by in-situ formation of the negative thermal expansion phases  $\text{ZrW}_2\text{O}_8$  and  $\text{Al}_2\text{W}_3\text{O}_{12}$ . The composition to achieve the lowest coefficient of thermal expansion according to the Turner model displayed the least amount of cracks in the laser-processed parts. Laser-manufactured parts using powders containing 50 vol% of  $\text{ZrO}_2/\text{WO}_3$  granules showed a compressive strength of 499 MPa and a Young's modulus of 100 GPa.

### 1. Introduction

Laser powder bed fusion (selective laser melting) provides new opportunities for design engineers to produce complex prototypes and small series in an expanded design space. The ability to manufacture ceramic parts by laser powder bed fusion could reduce the lead time on products while maintaining high accuracy. Furthermore, costs associated with the process of hard-machining and thermal post-processing could be minimized [1, 2]. The potential to increase efficiency of production using this technology would result in a more streamlined workforce. The medical industry, in which low-volume personalized components are often required for parts, such as dental crowns, artificial limbs and porous bone scaffolds [1] would

greatly benefit from these advantages. However, at this stage, the industrial usage of laser powder bed fusion to produce ceramic parts remains limited due to the brittle nature of this material group [2, 3].

Overcoming the challenges of low thermal shock resistance and weak densification of oxide ceramics in laser powder bed fusion was attempted by an optimization of the laser processing [1]. This covered tests of various laser types [4-9], exploring different laser scanning [10] and preheating strategies [5, 11-13] or by the combination of a self-healing material and a post-heat treatment step [14]. Another promising approach to establishing powder bed fusion - laser beam (PBF-LB) is to improve the mechanical properties of the parts through variation of the material composition combined with appropriate process developments (such as the addition of silica [4, 7, 15]). Additionally, the use of new materials provides opportunities to improve the absorptance of oxide ceramics such as aluminum oxide, which has a low absorption in the visible or near-infrared wavelength range (only 3% at 1064 nm [16]) [6]. Oxide powder absorptance of laser light in this range was previously increased by carbon [17], [18-21], SiC [20], Fe<sub>2</sub>O<sub>3</sub> [6, 22, 23] and MnO<sub>2</sub>/Mn<sub>2</sub>O<sub>3</sub> [24-26] and black TiO<sub>2-x</sub> [27] additions. These additions can be achieved through processes such as spray granulation. It provides the possibility of a homogeneous particle distribution within the powder bed even by using nano- or submicron powders [22]. Furthermore, high flowability of granules is favorable to achieve a high powder bed density. This method was adopted by Juste et al. [17], Mapar et al. [28, 29], Verga et al. [21], Liu et al. [30], Pfeiffer et al. [22, 26, 27] and Florio et al. [6, 25] to prepare the powder for the PBF-LB process.

Cracks in laser powder bed fusion of oxide ceramic parts are a result of the combination of a low thermal shock resistance and large thermal stresses that arise by a fast thermal expansion and shrinkage during rapid melting and re-solidification of the material. Furthermore, 3D printed materials are known to suffer from anisotropic thermophysical properties such as thermal expansion or thermal conductivity [31, 32]. These factors considerably limit the

mechanical strength of the produced high performance oxide ceramic parts by laser powder bed fusion, and therefore their use in mechanically demanding applications. This is the primary cause that laser powder bed fusion for oxide ceramics is not of interest for industrial applications. In general, other additive manufacturing methods as for example vat photopolymerization, stereolithography, binder jetting or material extrusion are preferred. Zhang et al. [33] and Zheng et al. [10] analyzed cracks in PBF-LB of high performance ceramics and they both distinguished between transverse cracks, those which run perpendicular to the scanning direction, and longitudinal cracks, those which run parallel to the scanning direction. Inter-granular fractures along the columnar crystals were predominant in both studies, however, trans-granular cracks were also observed. Zhang et al. [33] noticed that transverse cracks were primarily within the laser scan tracks and in the center of the specimen, while longitudinal cracks occurred mainly between scan tracks. A predominant location of cracks in between columnar crystals was also reported by Ferrage et al. [18] A high resolution tomography performed by Pfeiffer et al. showed that cracks are mainly located along the vertical (build) direction [26].

The main focus of previous research studies was on process parameter optimization to resolve the issue of crack formation. High temperature preheating using a second laser and induction heating enabled building parts with high mechanical strength in PBF-LB as shown by Wilkes [34], Hagedorn [12] and Liu [13] However, the required preheating temperature exceeded 1700°C and the non-uniform temperature profile (heat loss due to radiation, conduction and convection) caused cracks due to differences in volume expansion between the top and the bottom of the sample, for samples larger than 1 mm. Furthermore, the surface quality was poor due to uncontrolled sintering of the oxide powders at temperatures above 1700 °C. Mapar [29] achieved crack-free melting and re-solidification by using a large laser spot size (760 µm), high power (900 W) and speed (400 mm/s). However, the produced parts contained

a high porosity (about 30%), and their results are therefore less significant, since increasing crack formation is correlated to an increasing part density because of a larger buildup of stresses during cooling.

A solution to minimize thermal stresses in PBF-LB of high performance oxide ceramics could be the in-situ formation of a negative thermal expansion phase during processing to compensate and the resultant thermal expansion of the whole oxide ceramic composite is near zero. This phase expands during the cooling and counterbalances the shrinkage of the high performance oxide ceramic phase. One possibility is zirconium tungstate ( $\text{ZrW}_2\text{O}_8$ ), which exhibits an isotropic negative thermal expansion coefficient over an extended temperature range of 0.3 – 1050 K (coefficient of thermal expansions (CTE) of  $-8.7 \times 10^{-6} \text{ 1/K}$  for  $\alpha\text{-ZrW}_2\text{O}_8$  (20 – 430 K) and  $-4.9 \times 10^{-6} \text{ 1/K}$  for  $\beta\text{-ZrW}_2\text{O}_8$  (430 – 950 K)) [35, 36]. Upon heating, a phase transition from  $\alpha$ - to  $\beta\text{-ZrW}_2\text{O}_8$  occurs at about 150-155 °C. The effect of volume contraction is based on an open network structure (framework structure [37]). Anisotropic thermal vibrations are usually also present in other materials, but are typically dominated by other forces leading to a positive thermal expansion [36]. Zirconium tungstate is a metastable phase and can be achieved by rapid quenching, which is the case in the PBF-LB processes. The thermodynamically stable temperature zone is between 1105 and 1257 °C [38, 39]. Above 1257 °C  $\text{ZrW}_2\text{O}_8$  melts incongruently to  $\text{ZrO}_2$  and a liquid [40]. By rapid cooling, the decomposition into  $\text{WO}_3$  and  $\text{ZrO}_2$  is circumvented by conventional techniques [36] like quenching in air [41] or liquid nitrogen [42].

A challenge of  $\text{ZrW}_2\text{O}_8$  parts is the low mechanical strength due to high porosity (11.0 – 17.3% [42]), when produced with traditional processing methods. De Buysser et al. measured for pure  $\text{ZrW}_2\text{O}_8$  a 3-point bending strength of only 14 MPa [37]. Furthermore,  $\text{ZrW}_2\text{O}_8$  is in general unsuitable for high-temperature applications due to its instability between 600 to 1105 °C [35] and displays a rather large volume change at 155 °C due to the  $\alpha$ - to  $\beta$ -phase

transformation. In addition, the rule of mixture to estimate the CTE of composites containing this material could be not applied [37, 43] due to the low stiffness of  $\text{ZrW}_2\text{O}_8$  [43] and due to the voids and cracks within the parts [37, 44, 45]. Romao et al. [43] suggested to use the Turner model [46, 47] for prediction of the CTE for composites containing zirconium tungstate:

$$\alpha_c = \frac{\alpha_1 K_1 V_1 + \alpha_2 K_2 V_2}{K_1 V_1 + K_2 V_2} \quad (1)$$

$\alpha$  is the CTE,  $V$  is the volume fraction and  $K$  is the bulk modulus. The subscripts c, 1 and 2 refers to the final composite, the first phase (e.g.  $\text{ZrW}_2\text{O}_8$ ) and the second phase, respectively.  $\alpha\text{-Al}_2\text{O}_3$  was chosen in this work as a second phase, since it is high temperature stable with a low tendency for reaction, and should, in theory, avoid the formation of undesired phases and a rapid volume change during laser processing. Bulk modulus and thermal expansion values found in the literature are 13 GPa [41] and  $-4.9 \times 10^{-6}$  1/K for  $\beta\text{-ZrW}_2\text{O}_8$  [35] and 250 GPa [48] and  $8.1 \times 10^{-6}$  1/K [49] for  $\alpha\text{-Al}_2\text{O}_3$ . Applying the Turner model, a phase ratio of 96.9 vol%  $\text{ZrW}_2\text{O}_8$  to 3.1 vol%  $\text{Al}_2\text{O}_3$  was calculated to achieve an optimized resultant CTE of  $5.2 \times 10^{-8}$  1/K (near zero). Furthermore, a 50/50 vol% ratio was chosen as reference to enable a comparison of the properties of the laser processed parts. Properties of parts made from 99% pure aluminum oxide were already evaluated in the authors previous research [6, 22, 26].

Since  $\text{ZrW}_2\text{O}_8$  is transparent throughout the visible spectrum [35], a powder mixture of pure  $\text{WO}_3$  and  $\text{ZrO}_2$  (bandgaps of 2.6 eV [50] and 5.1 eV [51]) is required, in which  $\text{WO}_3$  sufficiently increases the absorptance of the powder for a successful PBF-LB process. It should be noted, that submicron- and micron-sized  $\text{ZrW}_2\text{O}_8$  powder is not commercially available. Thus far, zirconium tungstate has only been synthesized via laser processing using a  $\text{CO}_2$  laser [52], as both starting materials show a high absorption at the wavelength of the  $\text{CO}_2$  laser (10.6  $\mu\text{m}$ ) [53, 54]. However, the spot size, therefore the melt pool size depends on the used wavelength, which then limits the geometrical accuracy of  $\text{CO}_2$  lasers in additive manufacturing. The laser-processed samples showed an oriented growth of nano-crystallites relative to the temperature

gradient and primarily the high-pressure phase  $\gamma$ -ZrW<sub>2</sub>O<sub>8</sub>, indicating compressive stresses induced during solidification. A pure  $\alpha$ -ZrW<sub>2</sub>O<sub>8</sub> phase could be produced after annealing [52].

The focus of this study was particularly on minimizing cracks in the oxide ceramic components by in-situ formation of negative thermal expansion phases and not on surface quality optimization of the laser processed parts.

## 2. Experimental

### 2.1. Starting materials

Spray-dried granules were produced from ZrO<sub>2</sub> nanoparticles TZ-0 (Tosoh Corporation, Japan) and WO<sub>3</sub> nanoparticles (ALB Materials Inc, USA). These granules were mixed with coarse aluminum oxide AA18 (Sumitomo, Chemical Co. LTD, Japan) to achieve the desired powder compositions for laser processing and to increase the final powder bed density. The aim of this powder preparation was to achieve a counterbalancing of the shrinkage of alumina by the expansion of zirconium tungstate during cooling by homogeneous distribution of these two phases, therefore, an adjustment of the resultant thermal expansion coefficient of the produced part to near zero. This should be ensured by the introduction of the coarse-grained Al<sub>2</sub>O<sub>3</sub> particles, which have a low tendency for melting or for reacting with both nanoparticles within the spray dried granules to avoid undesired reaction-products during laser processing (e.g. AlWO<sub>4</sub> [55]), that have less suitable thermal expansion coefficient. Some of these undesired reaction-products also show an anisotropic thermal expansion and thus, easily develop microcracks below the consolidation temperature [35]. Ammonium citrate dibasic p.a. 98% (Sigma Aldrich Corp., USA) was used as a surfactant to modify the charges of the particle surfaces. A pH-value adjustment of the WO<sub>3</sub> nanoparticle dispersions was achieved through the use of a 10% diluted ammonium hydroxide solution (Carl Roth GmbH + Co. KG, Germany). The change of the pH-value was measured by the Five Easy Plus pH meter FP 20-Std-Kit (Mettler Toledo Schweiz GmbH, Switzerland).

Helium pycnometry (AccuPyc II 1340, Micromeritics, USA) was used to evaluate the absolute powder density. BET (Brunauer–Emmett–Teller) measurements (SA 3100, Beckman Coulter, Germany) provided the specific surface area (SSA). The need to degas the powders before performing the SSA measurement was eliminated by the utilization of synthetic air for two hours at 180 °C (SA-PREP Surface Area Outgasser, Beckman Coulter, Germany). The measured absolute density and SSA was used to calculate the corresponding BET average particle size according to the Sauter mean diameter [56]. The surface potential of the dispersed particles in water was measured using the electroacoustic zeta potential measurement method (ZetaProbe Analyzer, Colloidal Dynamics, USA) with an equilibration delay of 30 seconds. The measurements were performed at different pH-values to evaluate the saturation amount of surfactant on the particle surfaces. pH-adjustments of the suspensions (solid load of 5 wt%) were achieved by titration of a 0.1 molar HCl solution (Carl Roth GmbH + Co. KG, Germany) and a 0.1 molar NaOH solution (Sigma Aldrich Corp., USA). The dielectric constants were taken from [57]. The saturation amount of dispersant was mixed with each of the different powders to conduct a proper dispersion in Nanopure water. A combination of roll milling (24 hours) and vibration milling (20 min, vibrational frequency of 30 Hz) (Retsch MM301, Retsch GmbH, Germany) was utilized for the dispersion of the ZrO<sub>2</sub> particles. 0.4 mm ZrO<sub>2</sub> milling balls (Tosoh Corporation, Tokyo, Japan) were used for this dispersing routine. WO<sub>3</sub> particles were dispersed only by roll milling for 24 hours (1 mm ZrO<sub>2</sub> milling balls). Laser diffraction (LS 13320, Beckman Coulter GmbH, Germany) and dynamic light scattering (ZetaSizer Nano ZS, Malvern Panalytical Ltd, UK) provided the volume based particle size distributions of the dispersed particles in water. Refractive indexes and extinction coefficients required for the measurements were taken from [58] for WO<sub>3</sub> and [59] for ZrO<sub>2</sub>.



## 2.2. Spray granulation and mixing with coarse alumina

The mini spray dryer B-290 (Büchi Labortechnik AG, Switzerland) was utilized for spray granulation. The process was conducted with an ultrasonic atomizer in co-current mode. The supply of the spray drying slurry to the nozzle was accomplished by a peristaltic pump. This slurry was left stirring during spray drying to prevent demixing. Process parameters were an inlet temperature of 140 °C, an outlet temperature of ca. 100 °C, an air flow rate of 25 m<sup>3</sup>/h, a nozzle frequency of 60 kHz, a slurry feed rate of ca. 0.7 ml/min and an ultrasonic power of 4 W. The ultrasonic nozzle was prevented from overheating by a flow of compressed air. The process parameters were kept constant during spray drying. A cyclone with an attached collection vessel enabled the separation of the spray-dried granules from the gas stream. A final screening step (230 mesh (63 µm) sieve (Retsch GmbH, Germany)) of this powder led to the desired granule size distribution for laser processing. The yield of the granulation process was quantified by the fraction of the weight of obtained spray-dried granules to the weight of the solid content in the slurry mixed for spray drying. Finally, the desired powder compositions for PBF-LB were prepared by mixing 3.1 and 50 vol% of coarse aluminum oxide AA18 with the granules for 1 hour on a rolling bench.

Zirconium oxide and tungsten oxide powders were dispersed separately using the previously determined saturation amount of ammonium citrate dibasic of each powder prior to spray drying. 1 wt% (5 vol%) of binder PEG 35000 (Sigma Aldrich Corp., USA) was added prior to spray drying to the dispersed ZrO<sub>2</sub> particles after rotating for 20 hours to guarantee the formation of non-broken granules. After a homogenization step of two hours, the two slurry components were finally mixed for an additional two hours. The powder ratio in the slurry used for spray drying was 76.4 vol% (68 mol%) WO<sub>3</sub> and 23.6 vol% (32 mol%) ZrO<sub>2</sub> to achieve only the pure ZrW<sub>2</sub>O<sub>8</sub> phase according to the phase diagram [38, 39] after laser processing.



## **2.3. Powder characterization**

### **2.3.1. Apparent and tapped density, flowability and particle size distribution**

The apparent density of the powders (PTL Dr. Grabehorst GmbH, Germany) was measured according to the standard DIN EN ISO 23145-2 and the tapped density was quantified by tapping the powders 1000 times with a displacement of 3 mm in compliance to EN ISO 787-11 using a jolting volumeter (JEL STAVII, J. Engelsmann AG, Germany). Relative densities were quantified by the relations between apparent or tapped density to the absolute powder density. A flowability grading of the powders was performed by the Hausner ratio, which is defined as fraction of tapped density over apparent density. Values of this ratio below 1.25 indicate a fair flowability for the PBF-LB process [18, 20, 60, 61]. A Revolution Powder Analyzer (PS Prozesstechnik GmbH, Switzerland) was used to analyze the dynamic flow behavior during agitation. The avalanches of 10 ml powder in a rotating 25 ml drum (0.6 rounds/minute) were directly captured by a CCD camera and the characteristic values of the avalanche angle (angle of powder when an avalanche occurs) were automatically calculated by the integrated software (preparation time of 30 seconds). Three measurements with at least 127 avalanches were carried out. The lower the avalanche angle is, the better the powder flowability. Above an angle of 60°, it is difficult to achieve a suitable flowability for powder recoating, whereas an angle smaller than 60° implements a sufficient powder flowability to recoat a smooth powder layer [62]. Laser diffraction (LS 13320, Beckman Coulter GmbH, Germany) of the powders in isopropanol gave the volume based particle size distributions including the characteristic values for  $d_{10}$ ,  $d_{50}$  and  $d_{90}$ .

### **2.3.2. Electron microscopy and absorptance measurement**

Scanning electron microscopy (SEM) was used to visualize the  $\text{ZrO}_2$  and  $\text{WO}_3$  nanoparticles (Quanta 650 SEM, FEI, USA) and the mixed powders used for laser processing (SEM VEGA3 Tescan, Tescan, Czech Republic). Therefore, a thin powder layer was attached on an adhesive

carbon tab by the use of compressed air and finally sputtered with gold-palladium to enable the microscopy imaging. Element distributions within the granules were examined by energy-dispersive X-ray spectroscopy by the Bruker XFlash 6-10 detector (Bruker Corporation, USA). To visualize the internal structure of the granules by SEM, the granular material was cold embedded in a resin (CaldoFix-2, Struers GmbH, Switzerland). A thin powder layer was placed on the bottom of the embedding die and the resin was poured on top. Afterwards, the powder layer was ground, polished (with a 3  $\mu\text{m}$  diamond suspension) and finally sputtered with gold-palladium.

Qualitative light absorption measurements were conducted with an UV-VIS-NIR spectrophotometer (Shimadzu 3600, Shimadzu Corporation, Japan) applying the Kubelka-Munk method [63, 64]. The measurements were performed with 2 nm steps in a wavelength range of 300 - 1500 nm. More information to this method is given in [26]. This includes the calculation of the arbitrary constants of absorption coefficient  $K$  and scattering coefficient  $S$  by measuring the sample reflectance.

#### **2.4. Laser processing**

The customized powders were laser processed in a flexible PBF-LB setup built in-house at ETH Zurich [6]. A continuous wave IR fiber laser (redPOWER R4 200W, SPI Lasers, UK) with a wavelength of 1070 nm and a maximum output power of 200 W was used for laser processing. The optimized processing parameters were a spot size of 90  $\mu\text{m}$ , a hatch distance of 170  $\mu\text{m}$  and a layer thickness of 40  $\mu\text{m}$ . The used laser power and scan speed for each powder combination are stated in the result and discussion chapter. A Sn60Pb40-coated steel was used as substrate for laser powder bed fusion. More details on the preparation procedure of the substrate can be found in Verga et al [21].

## 2.5. Characterization of PBF-LB manufactured parts

The visual appearance of the PBF-LB printed parts was imaged by optical microscopy. The optical microscope SteREO Discovery.V20 (Carl Zeiss Microscopy, Germany) was used to evaluate the shape and the accuracy of the parts. The internal structure of the parts was observed with the optical microscope Keyence VHX 5000 (Keyence Corporation, Japan). Furthermore, the internal microstructure was imaged by the SEM VEGA3 Tescan. The parts were cold embedded in the CaldoFix-2 resin and the cross-sections were ground and polished (1  $\mu\text{m}$  diamond suspension) prior to microscopy imaging,

Water was used as liquid medium to ascertain the density according to the Archimedes principle. This density was related to the absolute densities of crushed laser manufactured parts measured by helium pycnometry to obtain a relative density of the part. The compression tests were performed using the Instron 8801 servohydraulic testing systems (Illinois Tool Works Inc., USA). Cylinders with a part diameter of ca. 5 mm and a length of ca. 8 mm were manufactured by PBF-LB, ground plane-parallel and polished (5  $\mu\text{m}$  finish) prior to the tests. The uniaxial compressive strength  $\sigma$  was calculated by the fraction of applied force  $F$  over the cross sectional area  $A$  of the cylinders:

$$\sigma = \frac{F}{A} = \frac{F}{\frac{1}{4}d^2\pi} \quad (2)$$

The Young's modulus of the PBF-LB manufactured samples was quantified by the ultrasonic method. The parts were ground plane-parallel and honey was used as a couple medium to enable a good coupling between sensors and sample. The ultrasonic measuring device Panametrics 5900 PR (Olympus K.K., Japan) provided longitudinal  $c_L$  (use of 4 MHz) and transverse  $c_T$  (use of 0.5 MHz) waves through the samples. The sound velocities of these waves were calculated from time-of-flight measurements determined by the software Ultrasound Imaging System

Version 2.2.c and material thickness measurements. The Young's modulus  $E$  were calculated by these sound velocities and the material density  $\rho$  as follows:

$$E = 4\rho c_T^2 \frac{\frac{3}{4} - \left(\frac{c_T}{c_L}\right)^2}{1 - \left(\frac{c_T}{c_L}\right)^2} \quad (3)$$

X-ray powder diffraction was performed on ground PBF-LB manufactured parts in Bragg–Brentano geometry using a Bruker AXS D8 ADVANCE diffractometer (Bruker Corporation, USA), which is equipped with a Cu-K $\alpha$  X-ray source. The diffraction data was determined in a  $2\theta$  range of 5–120° in 0.02° steps and 1 second exposure time per step. Crystallographic phases were identified using the TOPAS Bruker AXS software.

### 3. Results and Discussion

#### 3.1 Dispersion of starting powders in water

**Figure 1a and b** show the optical appearance of the ZrO<sub>2</sub> and WO<sub>3</sub> nanoparticles, respectively. The powders feature particles with a uniform size distribution in the nano range. The WO<sub>3</sub> powder had a yellow color, whereas the ZrO<sub>2</sub> powder appeared in a pure white color. The measured absolute densities and specific surface areas were 5.62 g/cm<sup>3</sup> and 14.4 m<sup>2</sup>/g for the ZrO<sub>2</sub> powder and 6.93 g/cm<sup>3</sup> and 7.9 m<sup>2</sup>/g for the WO<sub>3</sub> powder. These results gave calculated BET average particle sizes of 74 nm for the ZrO<sub>2</sub> particles and 110 nm for the WO<sub>3</sub> particles. The ZrO<sub>2</sub> powder consisted entirely of the monoclinic phase (Baddeleyite) according to X-ray diffraction (**Figure S4**). A phase content of 100% Krasnogorite was found for the WO<sub>3</sub> powders (**Figure S4**). Other phases were not present in both powders. The used aluminum oxide powder AA18 was already analyzed in terms of absolute density in our previous work [22]. The absolute densities, the SSA and the BET average particle size of the used powders are summarized in **Table 1**.

**Table 1:** Absolute densities, specific surface area and BET average particle size of raw powders

| Raw material                              | Al <sub>2</sub> O <sub>3</sub> AA18 | ZrO <sub>2</sub> TZ-0 | WO <sub>3</sub> particles |
|---|-------------------------------------|-----------------------|---------------------------|
| Absolute density [g/cm <sup>3</sup> ]     | 3.99                                | 5.62                  | 6.93                      |
| Specific surface area [m <sup>2</sup> /g] | < 0.1                               | 14.4                  | 7.9                       |
| BET average particle size [nm]            |                                     | 74                    | 110                       |

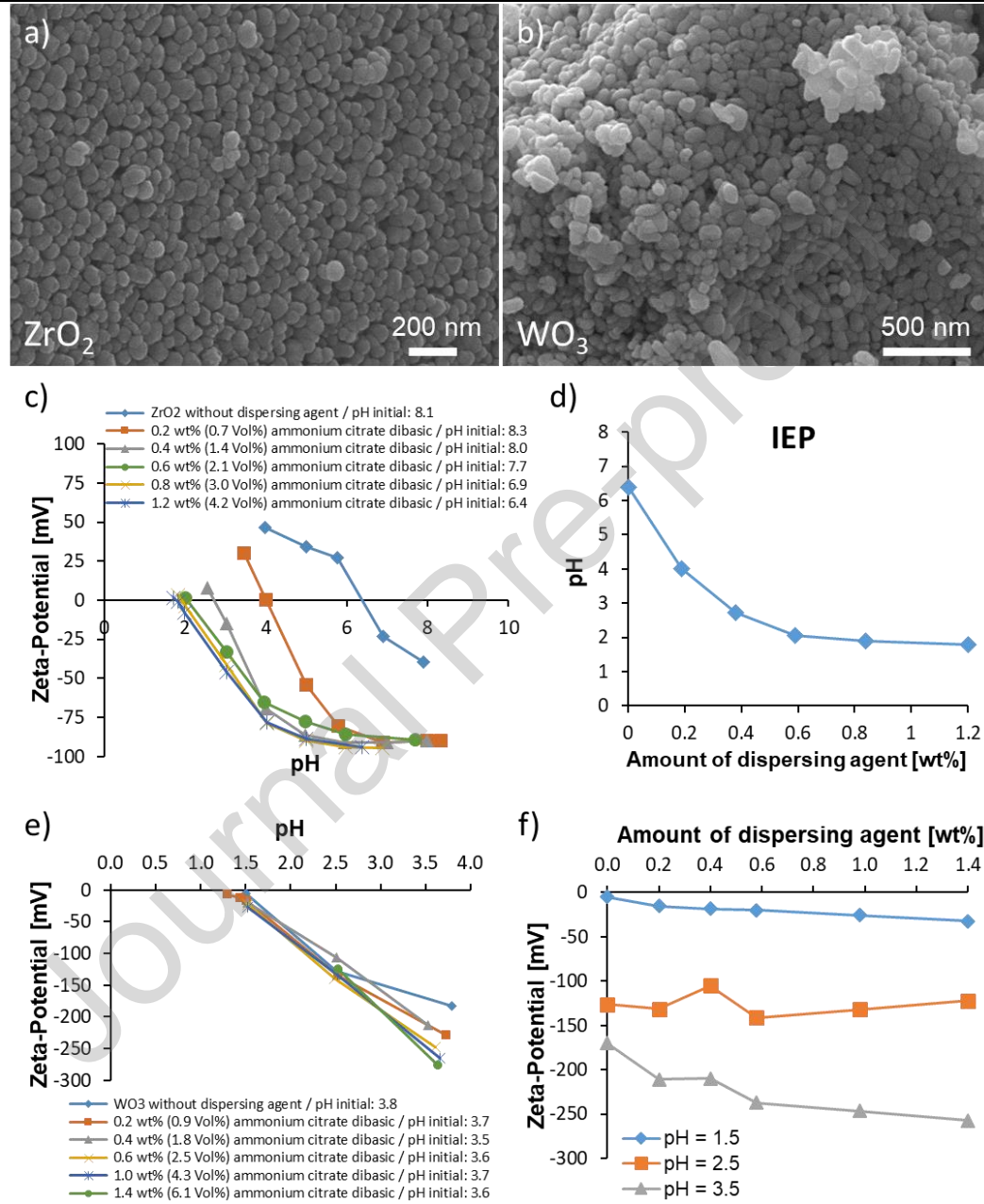


**Figure 1:** SEM images of agglomerated **a)** ZrO<sub>2</sub> and **b)** WO<sub>3</sub> nanoparticles. **c)** Zeta potential of ZrO<sub>2</sub> particles as a function of pH value and various citrate concentrations. **d)** pH<sub>IEP</sub> of ZrO<sub>2</sub> suspensions as function of ammonium citrate dibasic addition. **e)** Zeta potential of WO<sub>3</sub> particles as a function of pH value and various citrate concentrations. **f)** Zeta potential of WO<sub>3</sub> suspensions as function of ammonium citrate dibasic addition at constant pH values of 1.5, 2.5 and 3.5.

The zeta potential of the  $\text{ZrO}_2$  nanoparticles in water as a function of the pH value and various ammonium citrate concentrations is illustrated in **Figure 1c**. The addition of ammonium citrate dibasic shifts the isoelectric point from 6.4 to 1.8 (**Figure 1d**). Using the saturation amount of ammonium citrate dibasic (0.6 wt%/2.1 vol%), a zeta potential below -77 mV is created for pH values bigger than 5, which theoretically guarantees successful electrostatic stabilization of these particles in this pH range. By adsorption on the particle surfaces, the citrate causes an exchange of hydroxyl groups with carboxylate ions and creates a strongly negative charged surface, which enables a homogeneous dispersion. At the evaluated saturation amount, the surface of the particles should be already fully covered with a monolayer of citrate anions. **Figure 1e** shows the Zeta potential of the  $\text{WO}_3$  particles as a function of the pH value and the ammonium citrate addition. Since a dependency of the zeta was not clearly seen in this depiction, the zeta potential was represented as function of ammonium citrate dibasic addition at constant pH values of 1.5, 2.5 and 3.5 (**Figure 1f**). This depiction showed a decrease of the zeta potential by addition of ammonium citrate dibasic, especially for pH-values of 1.5 and 3.5, however, this decrease was only slight. Both powders ( $\text{ZrO}_2$  and  $\text{WO}_3$ ) are already negatively charged without using citrate, but zirconia has a much smaller zeta potential at the initial pH values (-40 mV to -180 mV). This means less repulsion on the carboxylate ions. However, this also explains the small shift of the zeta potential by use of this dispersant for  $\text{WO}_3$ . For further dispersion experiments with  $\text{WO}_3$ , an amount of 0.2 wt% (0.9 vol%) ammonium citrate dibasic was chosen, since a high zeta potential below -100mV was already present at pH values bigger than 2.5 and the change in the zeta potential was only small for bigger concentrations of the dispersing agent.

**Figure 2** summarizes volume based particle size distributions of  $\text{ZrO}_2$  and  $\text{WO}_3$  nanoparticles in water. Laser diffraction and dynamic light scattering confirmed agglomerations up to 2  $\mu\text{m}$  for different solid loadings when using only roll milling for 24 hours as a dispersing method for the  $\text{ZrO}_2$  particles. However, the particle size decreased significantly when

comparing to roll milling without a dispersant. Since attractive van der Waals forces have more impact on small nanoparticles due to gravitational forces decreasing with smaller particle size, these particles require an intensive dispersing step with higher energy input [66]. An additional vibration milling step for 20 min before roll milling shifted particles sizes to be smaller and destroyed bigger agglomerates. (**Figure 2a, b**). Furthermore, this enabled the preparation of suspensions with a high solid loading of 38.5 vol%. The lowest particles sizes with the characteristic values of d10, d50 and d90 of 104, 129 and 190 nm according to laser diffraction and of 105, 177 and 284 nm according to dynamic light scattering were measured for a solid load of 35 vol%. These values were close to the measured BET average particle size of 74 nm.

Achieving of a proper dispersion was not straight forward in the case of the  $\text{WO}_3$  particles. Without adjusting the pH value, agglomerations were observed at the initial pH values of 3.7 (0.2 wt% of ammonium citrate dibasic) and of 3.8 (no dispersant used), which could be due to a complete deprotonation of citrate at pH values of 3.5 – 4. Additional charges in the form of anions are not provided, but only neutral citric acid. A pH-value adjustment by a diluted ammonium hydroxide solution slowly improved the size distribution. At a pH range of 5.9 – 6.3 almost agglomeration free dispersions are shown in **Figure 2c and d**. The characteristic values of d10, d50 and d90 of 59, 83 and 129 nm according to laser diffraction and of 139, 216 and 309 nm according to dynamic light scattering were achieved using a solid load of 15 vol% and adjusting the pH to 5.9.

The volume based particle size distributions (LD) of the used alumina powder AA18 dispersed in water were already presented by Pfeiffer et al. [22, 26]. For this powder, the particle size distribution was only evaluated by laser diffraction, since the particle size was at the upper measurement limit of the dynamic light scattering device.

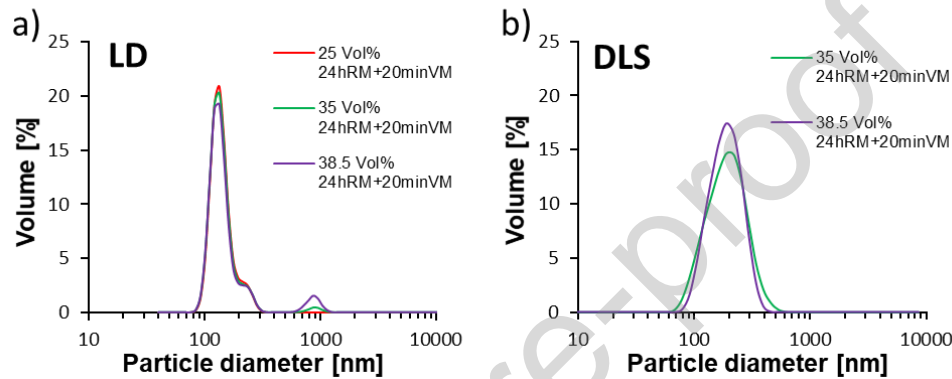
The results for the characteristic values of d10, d50 and d90 of the dispersed powders are summarized in **Table 2**.



**Table 2:**  $d_{10}$ ,  $d_{50}$  and  $d_{90}$  of volume based particle size distributions of dispersed powders in water determined by dynamic light scattering (DLS) and Laser diffraction (LD).

| Powder             | Al <sub>2</sub> O <sub>3</sub> AA18 | ZrO <sub>2</sub> TZ-0 | WO <sub>3</sub> particles |
|--------------------|-------------------------------------|-----------------------|---------------------------|
| Measurement method | LD                                  | LD                    | DLS                       |
| $d_{10}$           | 10.9 $\mu\text{m}$                  | 104 nm                | 105 nm                    |
| $d_{50}$           | 18.6 $\mu\text{m}$                  | 129 nm                | 177 nm                    |
| $d_{90}$           | 26.1 $\mu\text{m}$                  | 190 nm                | 284 nm                    |

### ZrO<sub>2</sub> particles



### WO<sub>3</sub> particles

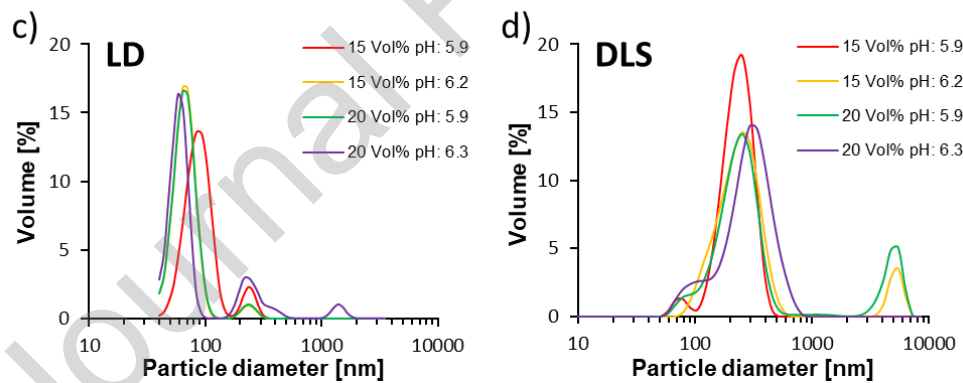


**Figure 2:** Volume based particle size distributions of ZrO<sub>2</sub> particles in water using an optimized dispersant amount of 0.6 wt% ammonium citrate dibasic dispersed by roll milling for 24 hours or a combination of vibration milling (20 minutes) and roll milling (24 hours) and determined by **a)** laser diffraction (LD) and **b)** dynamic light scattering (DLS). Volume based particle size distributions of WO<sub>3</sub> particles in water by optimized dispersant amount of 0.2 wt% dispersed by roll milling (24 hours) and determined by **c)** laser diffraction and **d)** dynamic light scattering.

## 3.2 Preparation of final powders for laser powder bed fusion

A detailed spray drying process parameter study was performed for the ZrO<sub>2</sub>/WO<sub>3</sub> granules.

The influence of the parameters was evaluated for slurry solid load, slurry feed rate (pump rate),

power output of the ultrasonic atomizer and inlet temperature of the spraying chamber. More information on this study can be found in the supplementary information (**Table S1 and Figure S1, S2, S3**).

#### A. Influence of solid load

A steady increase of the granule size by increasing the slurry solid load used for spray drying was observed. Differences between the granules made from different solid loads were not visible in SEM images. The solid load of 23 vol% was evaluated as the most suitable concentration, since it combined a high apparent and tapped density with the lowest Hausner ratio (i.e. best flowability).

#### B. Influence of slurry pump rate

A steady increase of the granule size was also seen by increasing the pump rate. The yield of spray drying was in a comparable range for all three pump rates. The same Hausner ratio for all three granules implied the same flowability for each, however, the highest apparent and tapped density were measured for a pump rate of 0.68 ml/min.

#### C. Influence of power output of ultrasonic nozzle

The sphericity of the granules was not affected up to a power of 8 W, but several broken and malformed granules with a non-uniform appearance as well as agglomerations were seen for a power of 20W. This loss of sphericity led to a decrease of the flowability (decrease of Hausner ratio); consequently, a strong decrease of the apparent and tapped density was observed.

#### D. Influence of inlet temperature

An inlet temperature of 140 °C was found as most favorable for apparent and tapped density of the granules. Furthermore, a good flowability and the highest yield was given for these granules. A clear trend for the granule sizes was not seen.

**Table 3** shows a short summary of the process parameter impact on granule size and shape. The final process parameters for spray drying chosen to produce the granules for laser powder

bed fusion were an ultrasonic power output of 4 W, a pump rate of 0.68 ml/min, a solid load of 23 vol% and an inlet temperature of 140 °C.

**Table 3:** Short overview of the results achieved in the process parameter study

| Process parameter                 | Additional information       | Effect on              |                       |
|-----------------------------------|------------------------------|------------------------|-----------------------|
|                                   |                              | Granule size           | Granule shape         |
| Solid load / Concentration        | ↑                            | ↑                      | (=)                   |
| Pump rate                         | ↑                            | ↑                      | (=)                   |
| Power output of ultrasonic nozzle | ↑ Changes only at high power | ↓                      | Shape distortions     |
| Inlet temperature                 | ↑                            | (=)                    | (=)                   |
|                                   |                              | (=) No effect observed | ↑ Increase ↓ Decrease |

SEM images of the  $\text{ZrO}_2/\text{WO}_3$  granules sprayed with the optimized process parameters are depicted in **Figure 3a and b**. The granules have a high sphericity with a homogeneous surface. This spherical shape was confirmed by a low Hausner ratio of 1.11 and a low avalanche angle of 34.9° leading to a smooth rearrangement of the powder bed surface. Furthermore, malformed granules were not present.

**Figure 3c** shows the element distribution within the granules determined by energy-dispersive X-ray spectroscopy. The three elements, tungsten, oxygen and zirconium, are uniformly distributed within the granules, which indicates a homogeneous distribution of the  $\text{WO}_3$  and  $\text{ZrO}_2$  particles. The calculated content of  $\text{ZrO}_2$  and  $\text{WO}_3$  was 22.1 wt% and 77.9 wt%, respectively, which was close to the desired eutectic ratio of 20/80 wt% (23.6/76.4 vol%).

**Figure 3d and e** show the inner structure of the spray-dried  $\text{ZrO}_2/\text{WO}_3$  granules. The granules have a very uniform microstructure and are solid without a hollow core. These observations confirm the results reported from Iskandar et al. [66]. Solid and dense granules made from silica were produced by using a high solid concentration, a high content of nanoparticles and a small droplet size [66].

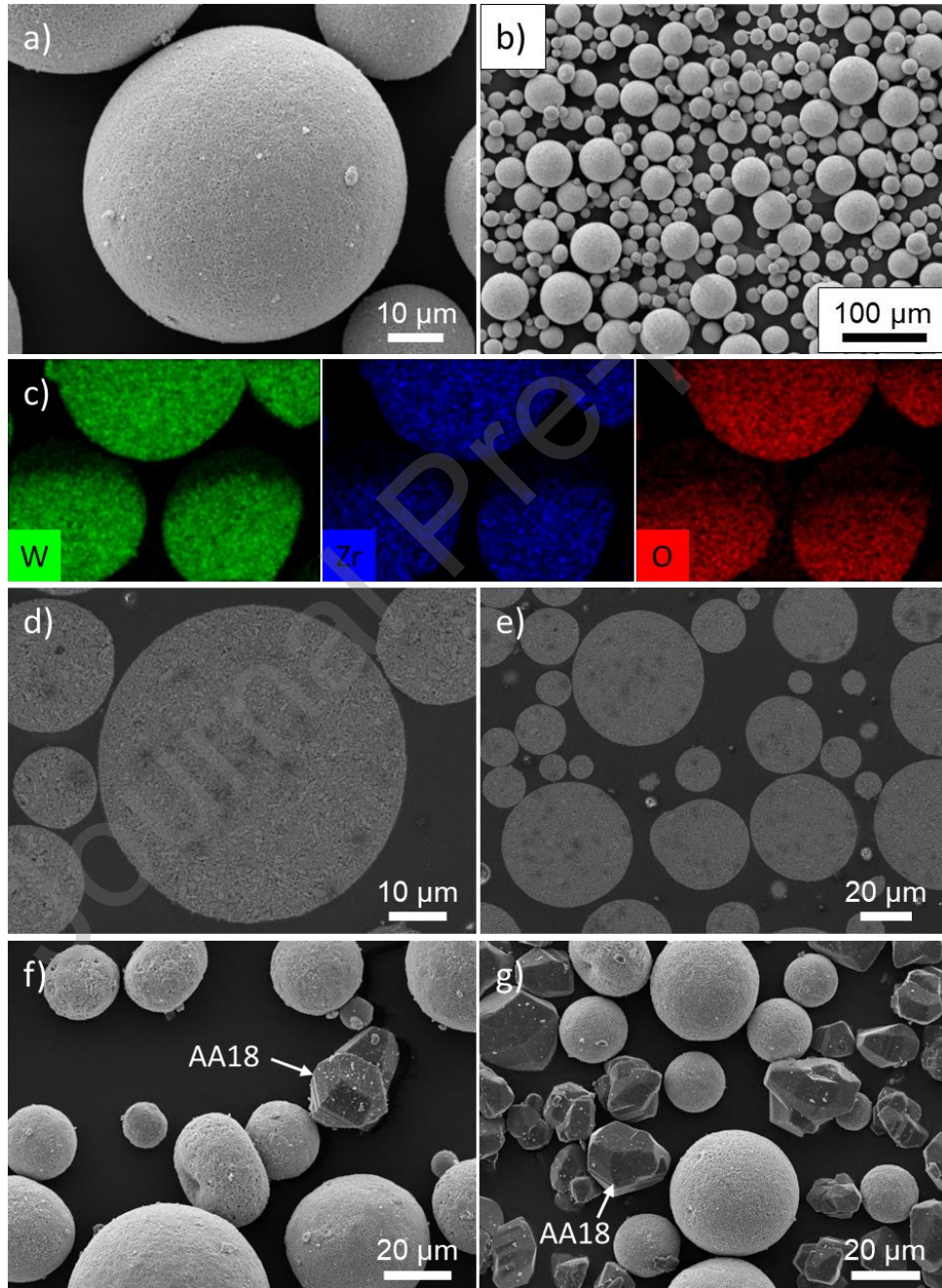


**Figure 3:** a), b) SEM images of  $\text{ZrO}_2/\text{WO}_3$  granules with corresponding c) element distributions of W, Zr and O examined by energy-dispersive X-ray spectroscopy within a granule and e), f) subsurface morphology of the granules. SEM images of the granules mixed with e) 3.1 vol% (powder combination A) and f) 50 vol% (powder combination B) coarse aluminum oxide AA18.

Two different ratios of  $\text{ZrO}_2/\text{WO}_3$  granules to coarse aluminum oxide powder were chosen in this work as discussed before (powder combination A: 96.9/3.1 vol% (Turner model) and powder combination B: 50/50 vol%). The different contents of coarse alumina AA18 could be homogeneously distributed within the  $\text{ZrO}_2/\text{WO}_3$  granules (**Figure 3f, g**). Furthermore, the granules were not destroyed during the mixing process.

**Table 4:** Properties of powders used for laser processing containing coarse alumina AA18 and spray dried  $\text{ZrO}_2/\text{WO}_3$  granules.

| Composition                 | Powder combination A<br>96.9 vol% granules + 3.1 vol%<br>alumina AA18 | Powder combination B<br>50 vol% granules + 50 vol%<br>alumina AA18 |
|-----------------------------|---|--|
| Apparent density in % of TD | $30.6 \pm 0,63$   | $38.3 \pm 0,16$  |
| Tapped density in % of TD   | $34.4 \pm 0,03$   | $44.3 \pm 0,28$  |
| Hausner ratio               | 1.13  | 1.16   |
| d10 in $\mu\text{m}$        | 16.8  | 11.6   |
| d50 in $\mu\text{m}$        | 33.5  | 21.0   |
| d90 in $\mu\text{m}$        | 53.0  | 42.2   |

**Table 4** summarizes the properties of the powders used for laser processing. Apparent and tapped density slightly decreased with the addition of the 3.1 vol% coarse alumina and then strongly increased again after adding 50 vol% coarse alumina (apparent and tapped density of pure granules are 31.2 and 34.7 % of TD). In contrary, the Hausner ratio of the powders increased by increasing the amount of coarse aluminum oxide, which indicates a flowability worsening. A similar behavior was also seen in the authors' previous work, which was attributed to the more irregular size distribution by adding the coarse alumina AA18 with minor particle sizes in the range of 10 - 30  $\mu\text{m}$  [22]. This impaired flow behavior effects a density decrease for a small alumina addition of 3.1 vol%, however, the decreased flowability does not have a big impact for an addition of 50 vol% of the densely packed AA18. In this case, the homogeneously distributed AA18 increases the apparent and tapped density.

The room temperature absorptance of the granules was evaluated by the Kubelka Munk method (**Figure 4**). The highest absorption was measured for pure  $\text{ZrO}_2/\text{WO}_3$  granules. The K/S ratio decreased over the completely measured wavelength (300 - 1500 nm) with the

addition of coarse aluminum oxide AA18. Furthermore, an increased absorptance was measured at the featured wavelength of the used continuous wave IR fiber laser (1070 nm). Pure AA18 did not show any visible absorption and therefore, it was not possible to process this powder by the used laser.

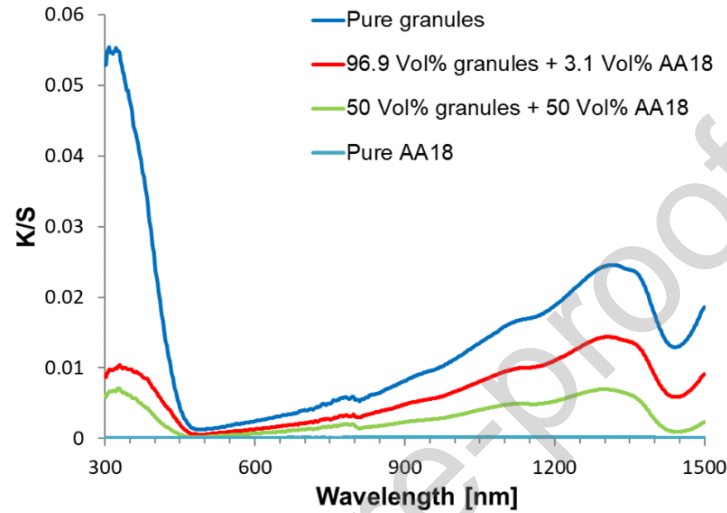


**Figure 4:** Qualitative absorption spectrum evaluated by Kubelka Munk method of pure granules, granules mixed with coarse aluminum oxide and pure coarse aluminum oxide AA18.

### 3.3 Laser manufacturing

Prior to PBF-LB, layers were directly consolidated by the IR laser on the top surface of uniaxially pressed cylindrical substrates containing pure  $\text{ZrO}_2/\text{WO}_3$  granules to evaluate the influence of the laser parameters on the  $\text{ZrW}_2\text{O}_8$  formation. X-ray diffraction measurements confirmed a formation of this phase in various amounts for selected laser processing parameters (Table 5).

**Table 5:** Evaluation of  $\text{ZrW}_2\text{O}_8$  phase after laser processing with different power outputs, hatch distances and laser speeds on uniaxially pressed cylindrical substrates containing pure  $\text{ZrO}_2/\text{WO}_3$  granules.

| Power [W] | hatch distance [μm] | laser speed [mm/s] | Power/speed [J/mm] | Energy density [J/mm <sup>2</sup> ] | Formation of $\text{ZrW}_2\text{O}_8$ |
|-----------|---------------------|--------------------|--------------------|-------------------------------------|---------------------------------------|
| 200       | 100                 | 3000               | 0.067              | 0.87                                | no                                    |
| 200       | 100                 | 2000               | 0.100              | 1.30                                | no                                    |
| 200       | 100                 | 1500               | 0.130              | 1.73                                | no                                    |
| 15        | 150                 | 25                 | 0.600              | 7.79                                | yes                                   |
| 7.6       | 150                 | 25                 | 0.304              | 3.95                                | yes                                   |



The experiments showed that high power to speed ratios and high energy densities are preferred for the formation of zirconium tungstate by laser processing, leading to higher temperatures and therefore more time to form  $\text{ZrW}_2\text{O}_8$  during cooling. Despite that it is possible to generate zirconium tungstate phase in these pre-experiments, the evaluated parameters cannot be directly transferred in the PBF-LB process, because the heat conduction through the uniaxially pressed cylinders is different. Liang et al. reported formation of  $\alpha\text{-ZrW}_2\text{O}_8$  [52], however, a  $\text{CO}_2$  laser was used for those experiments, and therefore, a different laser absorption of the  $\text{ZrO}_2$  and  $\text{WO}_3$  starting material was given. Furthermore, higher laser powers of 400-800W, lower laser scan speeds of 1-5 mm/s and a bigger laser spot size of 10.4 mm were applied by them. Thus, the power/speed ratios (80 - 800 J/mm) and energy densities (7.69 – 76.92 J/mm<sup>2</sup>) of laser processing were in a higher range.

These pre-experiments helped to find a suitable processing window for PBF-LB of both powder combinations (3.1 and 50 vol% aluminum oxide) to build 6 x 6 x 6 mm cubes.

The P-v graphs are shown in **Figure 5a, b**. In both cases, large spatter was observed around the build chamber after processing, especially for the 96.9:3.1 vol% ratio (powder combination A). This may be due to the low boiling point of tungsten oxide (1730 °C for  $\text{WO}_2$  and 1837 °C for  $\text{WO}_3$  [67]), which may lead to evaporation during processing with alumina and zirconia, both which have a much higher boiling point (>3000 °C). **Figure 5c** shows an example of the large amount of darker spatter generated by laser processing with 30 W of the granules containing zirconia and tungsten oxide mixed with 3.1 vol% coarse alumina. Such spatter was reduced at 15 W, therefore this power level was used for creating geometrical defined parts (**Figure 5e**). The strong spatter led to inaccuracies in the geometry, as the parts were about 1 mm smaller in height than the expected value. This may not be a significant problem for simple geometries, such as cubes or cylinders, as additional layers could be built to compensate for the lower height, but it significantly limits building complex geometries. This phenomenon was considerably less evident with the powder containing 50 vol% of alumina (powder combination



B), likely due to the smaller amount of low melting tungsten oxide. **Figure 5d-f** illustrates parts processed with powder combination A or B using different laser parameters (power, laser speed and hatch distance (h)).

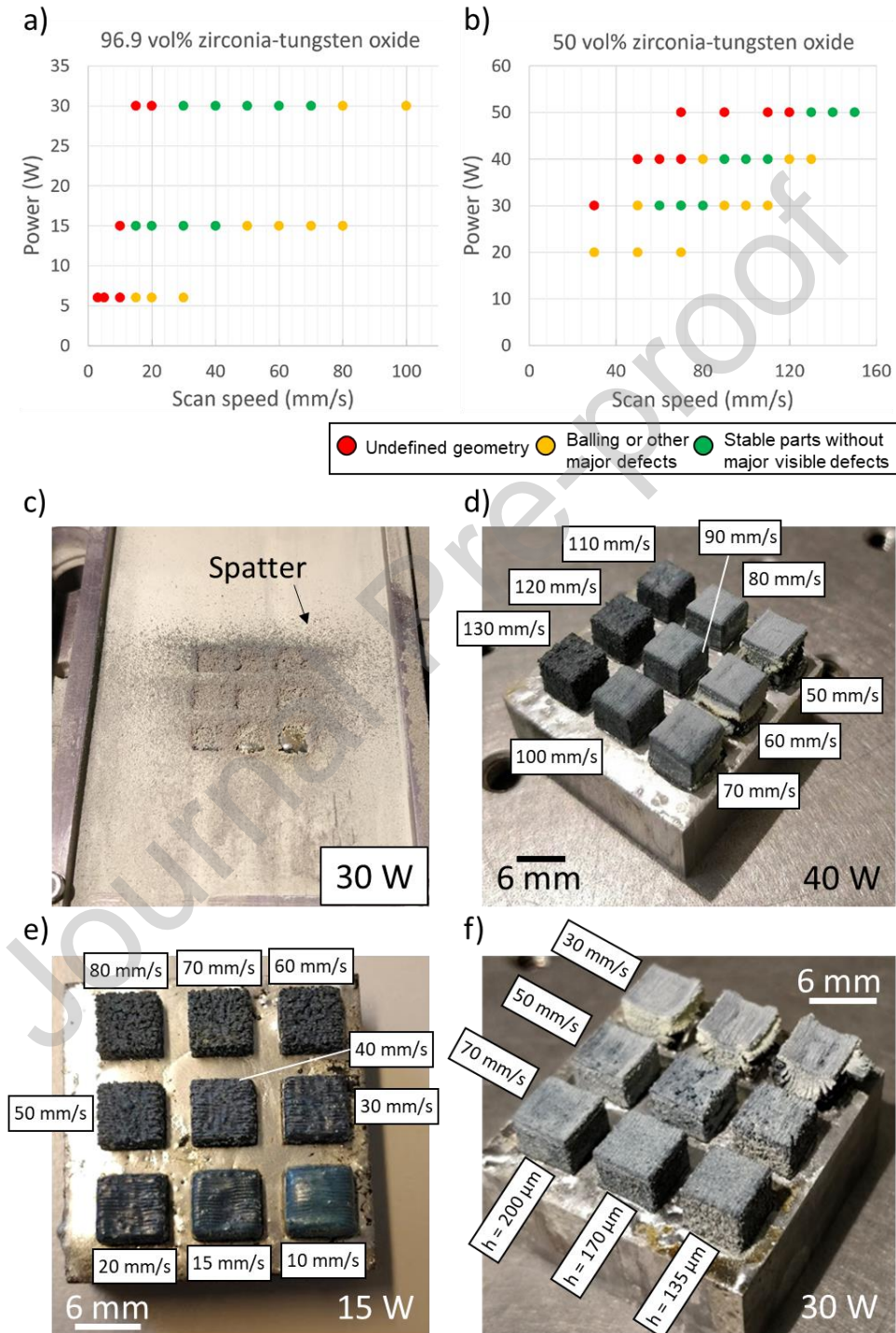


**Figure 5:** Process window for **a)** powder combination A from table 4 and **b)** powder combination B from table 4. **c)** Spatter generated around build chamber after laser processing with 30 W on 96.9 vol% zirconium tungsten oxide powder. Shape of parts processed with **d), f)** powder combination A and **e)** powder combination B using different laser parameters.

A laser power of 15 W and a scan speed of 30 mm/s for powder combination A and a laser power of 30 W and a scan speed of 70 mm/s for powder combination B were chosen for further processing, since the parts processed with these process parameters showed the highest density and geometrical accuracy. The hatch distance used in the experiments was 170  $\mu\text{m}$ . The spot size, layer thickness and substrate given in the experimental section were kept constant for both powders.

#### **Processing of powder combination A (from Table 4)**

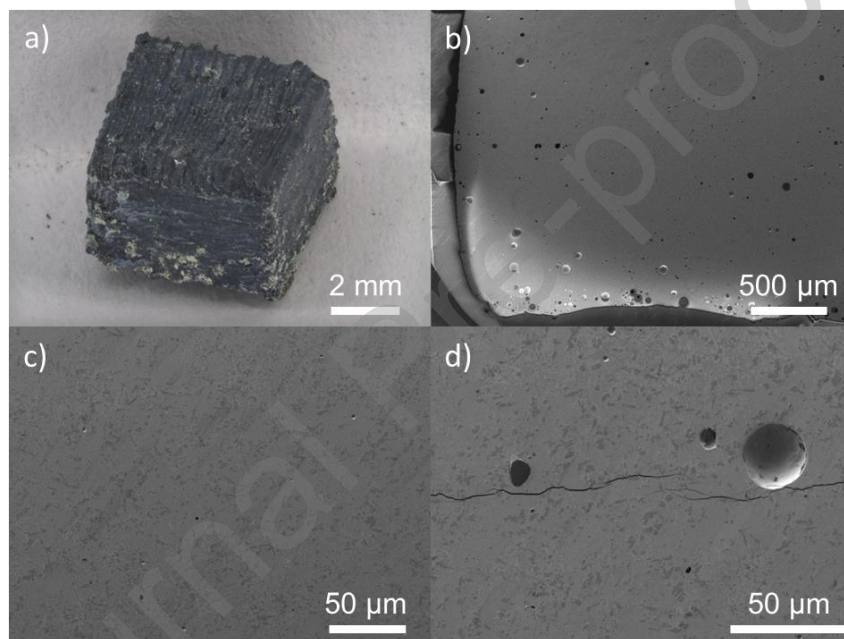


**Figure 6:** a) Shape imaged by optical microscopy and b-d) SEM images of cross-sections (top view) of laser-manufactured parts produced with powders containing 3.1 vol% coarse alumina AA18 and 96.9 vol% spray dried  $\text{ZrO}_2/\text{WO}_3$  granules

**Figure 6** shows laser-manufactured parts produced with powders containing 3.1/96.9 vol% aluminum oxide and  $\text{ZrO}_2/\text{WO}_3$  granules. The part shape shows a relatively low lateral and vertical accuracy due to the severe spatter effect explained earlier (**Figure 6a**). The part density measured in accordance to the Archimedes principle was 95.7%. Laser-induced cracks were not visible in low magnifications of the microstructure (**Figure 6b, c**). Vast regions without cracks were observed. At higher magnifications a few cracks were revealed (**Figure 6d**). Spherical porosity was also present, probably caused by local evaporation of tungsten oxide.

Crack reduction in these parts was achieved by the generation of the negative thermal expansion phase zirconium tungstate ( $\text{ZrW}_2\text{O}_8$ ) [35, 36], which was produced due to rapid cooling during laser processing. This rapid quenching prevents in general the decomposition of this phase into  $\text{WO}_3$  and  $\text{ZrO}_2$  [36, 42]. Thermal stresses were minimized due to the presence of a negative thermal expansion phase, since it expanded during cooling generating compressive stresses, which compensated the tensile stresses generated by the shrinking of aluminum oxide. The formation of  $\text{ZrW}_2\text{O}_8$  was confirmed by X-ray diffraction measurements of crushed parts (**Figure 7**). However, a complete transformation of zirconium oxide and tungsten oxide to zirconium tungstate was not obtained during laser processing. Residual tungsten oxide and zirconium oxide were still present in the material, which could be from unreacted  $\text{ZrO}_2/\text{WO}_3$  granules or produced by the decomposition process of  $\text{ZrW}_2\text{O}_8$  during cooling. Aluminum oxide reacted with tungsten oxide to result in a minor phase of aluminum tungstate.

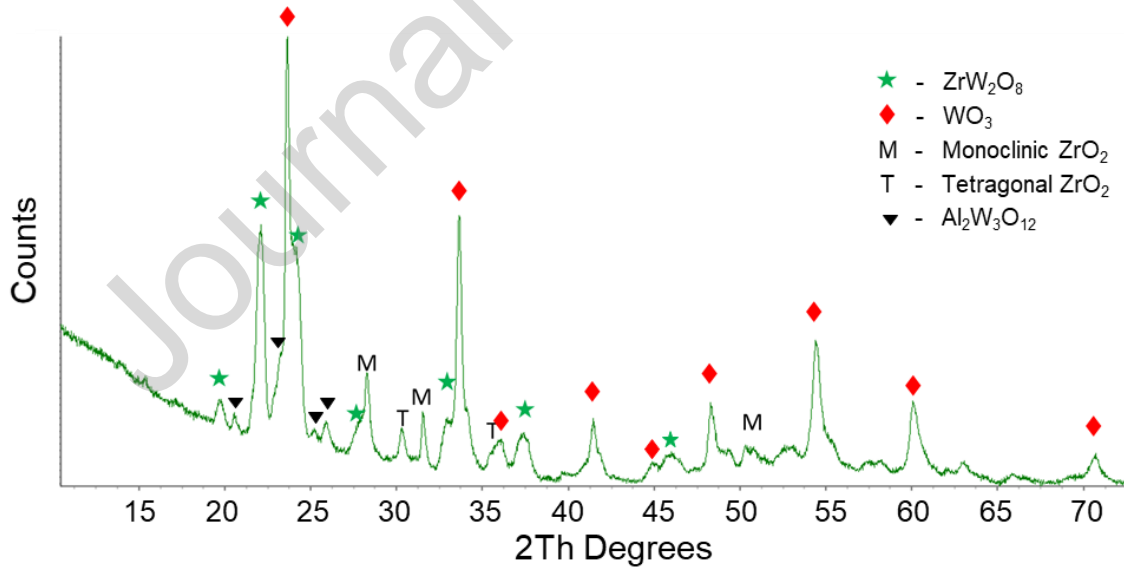


**Figure 7:** X-ray diffraction measurements of laser processed parts made from powder combination A

The optimized phase ratio of 96.9/3.1 vol% of  $\text{ZrW}_2\text{O}_8/\text{Al}_2\text{O}_3$  according to the Turner model ( $\text{CTE} = 5.2 \times 10^{-8} \text{ 1/K}$ ) led to a very low amount of cracks, as suggested by Romao et al. [43].



### Processing of powder combination B (from Table 4)

**Figure 8** shows optical microscope and SEM images of cross-sections (build direction (**a-d**) and top view (**e-h**)) of laser-manufactured parts produced from powders containing 50/50 vol% alumina and  $\text{ZrO}_2/\text{WO}_3$  granules.

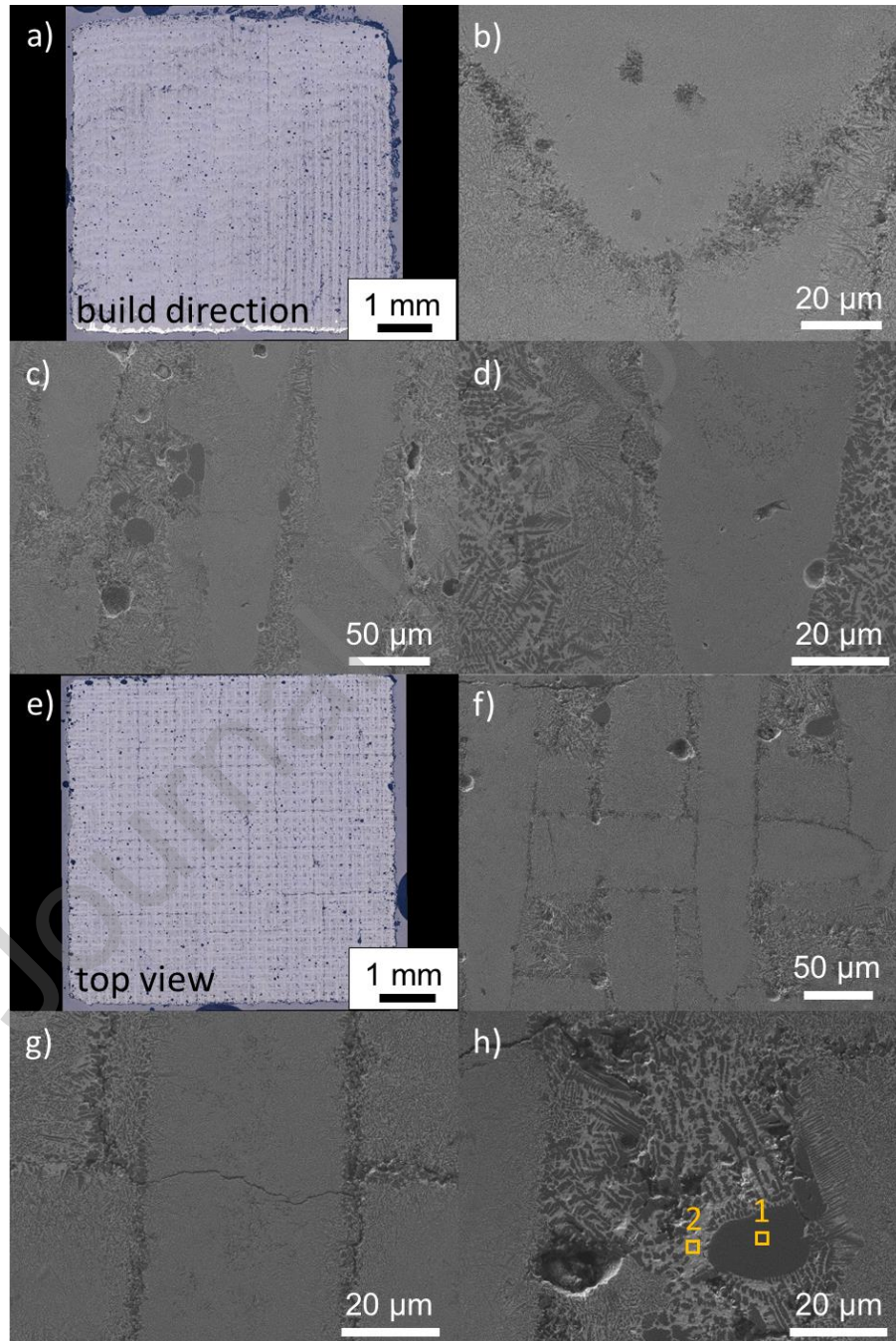


**Figure 8:** **a)** Optical microscope and **b-d)** SEM images of cross-sections (build direction) as well as **e)** Optical microscope and **f-h)** SEM images of cross-sections (top view) of laser-manufactured parts produced with powder combination B from Table 4 (positions evaluated for element content are marked in orange in **Figure 8h**).

The qualitative impression showed, that the shape of the parts had a relatively high lateral accuracy. The parts offered a high part density of 95.7% with a low amount of  $\mu\text{m}$ -sized circular pores, which confirms a suitable IR laser light absorptance of the used powder and the created melt pool. The spherical pores were probably formed due to local evaporation of tungsten oxide. Laser-induced cracks were hardly visible in the internal structure of these cross sections. However, a higher amount of micro-cracks was visible compared to parts processed with powder combination A (**Figure 8**). Furthermore, the microstructure contained different lamellar structures after laser processing (**Figure 8d**). These structures were also seen by other researchers upon laser processing of material systems with more components. Zhang et al. [33] and Zheng et al. [10] noticed that lamellar structures were generated along the build direction by thermal capillary convection (influenced by the Marangoni effect, streak convection and flowing Bénard cells). Liu et al. [30] obtained different rod-like lamellar eutectic structures during laser manufacturing of  $\text{Al}_2\text{O}_3/\text{GdAlO}_3/\text{ZrO}_2$  ternary ceramics.

The top-view cross-sections revealed uniform, consolidated laser scan tracks of ca. 50  $\mu\text{m}$ , which are smaller than the used laser spot size of 90  $\mu\text{m}$  (**Figure 8f, g**). The difference in distance maybe explained by the fact that the melt pool depth exceeds the layer depth and therefore, the tracks may be visible in different layers. These scanning tracks are surrounded by squares consisting of the already described lamellar structure. The origin of this unique microstructure could be due to the temperature differences within the melt pool, where the higher temperatures are located in the laser spot center. Furthermore, it could be that scan tracks from upper layers are visible, since the melt pool is usually deeper than a single layer.

The bright and dark phases within the lamellar structure were further analyzed by energy-dispersive X-ray spectroscopy (EDX) (**Figure 8h**). The element distribution (Al: 51.2 wt%; O: 48.8 wt%) within the dark phase (position 1) strongly indicates an aluminum oxide phase. This phase could be a non-molten AA18 particle considering the size of ca. 20  $\mu\text{m}$ . The surrounding bright phase (position 2) contains 37.8 wt% of Zr, 26.9 wt% of W, 28.9 wt% of O and 6.3 wt%

of Al. However, this measurement is not suitable to clearly indicate this surrounding phase. Therefore, x-ray diffraction measurements were performed to determine the existing phases in the laser processed part (**Figure 9**). Instead of a  $\text{ZrW}_2\text{O}_8$  phase from powder combination A, an  $\text{Al}_2\text{W}_3\text{O}_{12}$  phase was formed in-situ during laser processing, which could be the surrounding phase seen in the SEM analysis. The phase stability of  $\text{Al}_2\text{W}_3\text{O}_{12}$  was increased, since more  $\text{Al}_2\text{O}_3$  was present in this powder combination for the in-situ reaction. Furthermore, unreacted tungsten oxide, zirconium oxide and aluminum oxide were still present. As described above, residual tungsten oxide and zirconium oxide could be also created by decomposition of  $\text{ZrW}_2\text{O}_8$  during cooling

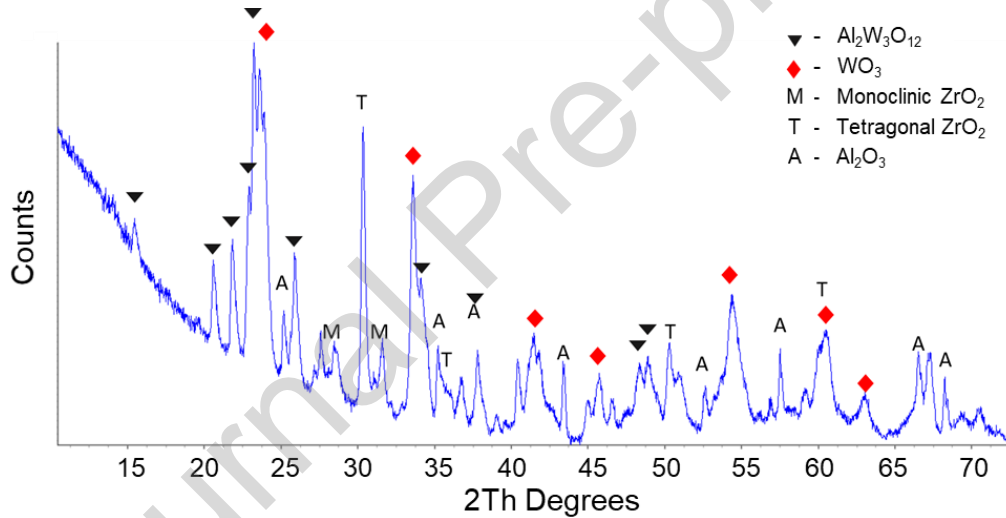


**Figure 9:** X-ray diffraction measurements of laser processed parts made from powder combination B

Crack reduction in the parts made from powder combination B is achieved by the in-situ formation of uniformly distributed aluminum tungstate ( $\text{Al}_2\text{W}_3\text{O}_{12}$ ) during laser processing. The exact value of the thermal expansion coefficient of this phase is controversially discussed in the literature, however, an anisotropic thermal expansion in different dimensions was reported in several works [68-70]. An anisotropic thermal expansion with a negative CTE along the a and c axes, but a positive CTE along the b axis was reported by Woodcock et al. (volumetric CTE of  $1.5 \times 10^{-6}$  1/K) [68] and by Imanaka et al. (volumetric CTE of  $1.2 \times 10^{-6}$  1/K) [72]. Achary et al. measured a negative linear thermal expansion coefficient in the region

of 25 to 850 °C of  $-1.5 \times 10^{-6}$  1/K [71]. Evans measured even different values for the CTE from dilatometer studies ( $-3 \times 10^{-6}$  1/K) and diffraction studies ( $2.2 \times 10^{-6}$ ) [69]. The controversy of the values was explained by Achary et al. by the influence of micro-cracks and defects on the CTE [71]. However, all of the evaluated thermal expansion coefficients are closer to zero than the CTE of  $\text{ZrW}_2\text{O}_8$ , which makes  $\text{Al}_2\text{W}_3\text{O}_{12}$  (powder combination B) less effective to reduce cracking in the laser processed oxide ceramic parts compared to the previously described  $\text{ZrW}_2\text{O}_8$  formation (powder combination A). Furthermore, Prisco et al. achieved a maximum 4-point bending strength of only 10 MPa for pure  $\text{Al}_2\text{W}_3\text{O}_{12}$  ceramics [72]. However, aluminum tungstate also offers a low Young's modulus (up to 91 GPa depending on grain size and porosity [72, 73]), which is in combination with the low thermal expansion coefficient very beneficial for avoiding crack formation.

Powder combination A and B showed both a large reduction of cracks compared to parts produced by Juste et al. [25] using 0.1 vol% graphite containing alumina granules as well as Pfeiffer and Florio et al. [6, 22, 26] using alumina granules with an iron oxide and manganese oxide doping below 1 vol%.

### 3.4 Mechanical properties

Severe crack formation due to thermal stresses during the rapid cooling in laser processing of pure aluminum oxide leads in general to a severe strength reduction. The in-situ formation of negative thermal expansion phases is an effective way to reduce the crack formation and therefore, to achieve improved compressive strength values. A compressive strength of  $498.9 \pm 89.3$  MPa was achieved by laser processing of powders consisting of 50/50 vol% spray-dried  $\text{ZrO}_2/\text{WO}_3$  granules and aluminum oxide (powder combination B). This value was higher than the value ( $327.9 \pm 52.1$  MPa) for powder combination B (96.9/3.1 vol%  $\text{ZrO}_2/\text{WO}_3$  granules and aluminum oxide), despite having more cracks after laser processing. The higher amount of the ternary phase with a low mechanical strength leads to a low compressive strength in the



final part. Reference compression strength values evaluated in the authors previous research [6, 22, 26] for parts processed by a nano-second pulsed green Nd-YAG laser made of 99% pure aluminum oxide doped with nano iron oxide or manganese oxide were 219 and 191 MPa, respectively. In comparison, compression strengths of conventionally sintered aluminum oxide parts can be more than 4000 MPa [74] (depending on the used grain size, purity of the raw material and the production method).

A Young's modulus of 99.7 GPa was achieved for parts made from powder combination B. This Young's modulus was higher than the 51.3 GPa for parts processed from powder combination A. The low values may be explained by the residual porosity present in the parts and the high amount of  $\text{ZrW}_2\text{O}_8$  and  $\text{Al}_2\text{W}_3\text{O}_{12}$  phases, which have low Young's moduli (88 GPa for single crystal  $\text{ZrW}_2\text{O}_8$  (average-over-direction) [75] and 91 GPa for spark plasma sintered  $\text{Al}_2\text{W}_3\text{O}_{12}$  ceramics (96% of TD [73]) compared to aluminum oxide (410 GPa [3]), zirconium oxide (monoclinic: 243 GPa and tetragonal: 212 GPa [76]) and tungsten oxide (305 GPa [77]). Parts made from powder combination A showed a lower Young's modulus, since they contained a much higher phase content of the in-situ formed ternary phase. In comparison, effective Young's moduli of traditionally manufactured  $\text{ZrW}_2\text{O}_8$  parts (strongly reduced by apparent porosity [3]) were only between 4.2 [42] and 4.3 GPa [41]. A similar dependency of the Young's modulus on the porosity was reported by Jardim et al. for  $\text{Al}_2\text{W}_3\text{O}_{12}$  ceramic parts [78]. The Young's moduli of those traditionally manufactured parts decreased linearly from 54 to 35 GPa in a porosity range from 10 to 25%.

#### 4. Conclusions

The in-situ formation of negative thermal expansion phases offers a suitable solution to reduce crack formation due to thermal stresses in laser powder bed fusion of aluminum oxide.

Since the ternary phase  $\text{ZrW}_2\text{O}_8$  was desired in the final laser processed parts, a powder consisting of spray-dried  $\text{ZrO}_2/\text{WO}_3$  granules and coarse alumina particles (less prone to

melting) was developed. A proper particle dispersion led to a uniform distribution of tungsten oxide and zirconium oxide in the granules, which was confirmed by energy-dispersive x-ray spectroscopy. The final powders were mixed with the ratio of 96.9/3.1 vol% of  $\text{ZrO}_2/\text{WO}_3$  to  $\text{Al}_2\text{O}_3$  (to achieve the lowest possible CTE of  $5.2 \times 10^{-8} \text{ 1/K}$  according to the Turner model) and with a ratio of 50/50 vol%  $\text{Al}_2\text{O}_3$  to  $\text{ZrO}_2/\text{WO}_3$  granules. The addition of granules increased the room temperature absorptance at the wavelength of the used IR fiber laser (1070 nm).

In laser-manufactured parts made from 50/50 vol% coarse alumina and  $\text{ZrO}_2/\text{WO}_3$  granules, an  $\text{Al}_2\text{W}_3\text{O}_{12}$  phase was discovered. Parts with this in-situ formed phase showed a strong reduction in crack formation. A lamellar structure created due to temperature differences within the melt pool was noticed in the microstructure. The optimized ratio according to the Turner model of 96.9/3.1 vol% revealed an even lower amount of cracks in the laser manufactured parts. Sufficiently high energy densities led to formation of the negative thermal expansion  $\text{ZrW}_2\text{O}_8$  phase within these parts. Vast regions without cracks were visible in low magnifications of the microstructure and only higher magnifications revealed a small amount of cracks. The highest compressive strength of  $498.9 \pm 89.3 \text{ MPa}$  and a Young's modulus of 99.7 GPa was achieved by using the 50/50 vol% powder combination. The compressive strength was higher than for the 96.9/3.1 vol% powder mixture, despite a larger amount of cracks due to the lower strength and larger amount of the negative thermal expansion phase.

The formation of ternary oxides was shown in this work as an effective way to reduce the crack formation. However, too much the ternary phase can reduce the final strength of the parts, despite the positive effect on the thermal stresses. Further investigations can be focused to find an optimal content to reduce cracks without significantly reducing the properties of the printed parts.

The proposed approach of creating negative thermal expansion phases during PBF-LB to minimize the formation of cracks could also be expanded to other ceramics systems. In the case

of zirconia, not only tungsten oxide would be a suitable additive, but also hafnium oxide (HfO<sub>2</sub>) and vanadium oxide (V<sub>2</sub>O<sub>5</sub>) could be of interest to form the negative thermal expansion materials hafnium vanadate (HfV<sub>2</sub>O<sub>7</sub>) or zirconium vanadate (ZrV<sub>2</sub>O<sub>7</sub>) during the process [35]. However, the biggest disadvantage of using this material system, is that vanadium(V) oxide is a toxic material. Furthermore, other interesting phases for systems containing WO<sub>3</sub> could be hafnium tungstate (HfW<sub>2</sub>O<sub>8</sub>), or scandium tungstate (Sc<sub>2</sub>W<sub>3</sub>O<sub>12</sub>) with a CTE of  $-11 \times 10^{-6}$  1/K and near isotropic thermal expansion [35].

### Acknowledgements

An exceptional thank goes to the ETH Board for funding the “FUORCLAM” project within the frame of the SFA (Strategic Focus Areas) Advanced Manufacturing. The authors thank Dr. Amy Knorpp, John Northridge and Bryan Lee for proofreading the text and Dr. Sena Yüzbaşı for IT-support. Furthermore, special thanks to Roman Furrer (Empa Dübendorf) for conducting the sound velocity measurements to determine the Young's modulus and Dr. Evgeniia Gilshtein (Empa Dübendorf) for SEM measurements of the ceramic nanoparticles.

### References

- [1] S. Pfeiffer, K. Florio, D. Puccio, M. Grasso, B.M. Colosimo, C.G. Aneziris, K. Wegener, T. Graule, Direct laser additive manufacturing of high performance oxide ceramics: A state-of-the-art review, *J. Eur. Ceram. Soc* 41(13) (2021) 6087-6114.
- [2] A. Zocca, P. Colombo, C.M. Gomes, J. Günster, Additive Manufacturing of Ceramics: Issues, Potentialities, and Opportunities, *J. Am. Ceram. Soc.* 98(7) (2015) 1983-2001.
- [3] H. Salmang, H. Scholze, *Keramik*, Springer-Verlag Berlin Heidelberg Berlin Heidelberg 2007.
- [4] A. Gahler, J.G. Heinrich, J. Günster, Direct laser sintering of Al<sub>2</sub>O<sub>3</sub>-SiO<sub>2</sub> dental ceramic components by layer-wise slurry deposition, *Journal of the American Ceramic Society* 89(10) (2006) 3076-3080.
- [5] J. Deckers, S. Meyers, J.P. Kruth, J. Vleugels, Direct selective laser sintering/melting of high density alumina powder layers at elevated temperatures, *Physics Procedia* 56 (2014) 117-124.
- [6] K. Florio, S. Pfeiffer, M. Makowska, N. Casati, F. Verga, T. Graule, H. Van Swygenhoven, K. Wegener, An innovative selective laser melting process for hematite-doped aluminum oxide, *Advanced Engineering Materials* 21(6) (2019).
- [7] P. Regenfuss, A. Streek, L. Hartwig, S. Klötzer, T. Brabant, M. Horn, R. Ebert, H. Exner, Principles of laser micro sintering, *Rapid Prototyping Journal* 13(4) (2007) 204-212.
- [8] Z. Fan, M. Lu, H. Huang, Selective laser melting of alumina: A single track study, *Ceramics International* 44(8) (2018) 9484-9493.
- [9] J. Liu, S. Bai, Femtosecond laser additive manufacturing of YSZ, *Appl. Phys. A* 123(4) (2017).
- [10] Y. Zheng, K. Zhang, T.T. Liu, W.H. Liao, C.D. Zhang, H. Shao, Cracks of alumina ceramics by selective laser melting, *Ceram. Int.* 45(1) (2019) 175-184.

- [11] S. Buls, J. Vleugels, B. Van Hooreweder, Microwave assisted selective laser melting of technical ceramics, Annual international solid freeform fabrication symposium - an additive manufacturing conference 29 (2018) 2349-2357.
- [12] Y.-C. Hagedorn, J. Wilkes, W. Meiners, K. Wissenbach, R. Poprawe, Net shaped high performance oxide ceramic parts by selective laser melting, *Physics Procedia* 5 (2010) 587-594.
- [13] Q. Liu, Y. Danlos, B. Song, B. Zhang, S. Yin, H. Liao, Effect of high-temperature preheating on the selective laser melting of yttria-stabilized zirconia ceramic, *Journal of Materials Processing Technology* 222 (2015) 61-74.
- [14] F. Verga, M. Makowska, G. Cellerai, K. Florio, M. Schmid, K. Wegener, Crack-healing, a novel approach for a laser-based powder bed fusion of high-performance ceramic oxides, *Additive Manufacturing Letters* 1 (2021) 100021.
- [15] B.H. Bae, J.W. Lee, J.M. Cha, I.-W. Kim, H.-D. Jung, C.-B. Yoon, Preliminary Characterization of Glass/Alumina Composite Using Laser Powder Bed Fusion (L-PBF) Additive Manufacturing, *Materials* 13(9) (2020) 2156.
- [16] N.K. Tolochko, Y.V. Khlopkov, S.E. Mozzharov, M.B. Ignatiev, T. Laoui, V.I. Titov, Absorptance of powder materials suitable for laser sintering, *Rapid Prototyping Journal* 6(3) (2000) 155-161.
- [17] E. Juste, F. Petit, V. Lardot, F. Cambier, Shaping of ceramic parts by selective laser melting of powder bed, *Journal of Materials Research* 29(17) (2014) 2086-2094.
- [18] L. Ferrage, G. Bertrand, P. Lenormand, Dense yttria-stabilized zirconia obtained by direct selective laser sintering, *Additive Manufacturing* 21 (2018) 472-478.
- [19] S. Chang, L. Li, L. Lu, J.Y.H. Fuh, Selective laser sintering of porous silica enabled by carbon additive, *Materials* 10(11) (2017).
- [20] L. Moniz, C. Colin, J.-D. Bartout, K. Terki, M.-H. Berger, Laser beam melting of alumina: Effect of absorber additions, *Jom* 70(3) (2018) 328-335.
- [21] F. Verga, M. Borlaf, L. Conti, K. Florio, M. Vetterli, T. Graule, M. Schmid, K. Wegener, Laser-based powder bed fusion of alumina toughened zirconia, *Additive Manufacturing* 31 (2020).
- [22] S. Pfeiffer, K. Florio, M. Makowska, D. Ferreira Sanchez, H. Van Swygenhoven, C.G. Aneziris, K. Wegener, T. Graule, Iron oxide doped spray dried aluminum oxide granules for selective laser sintering and melting of ceramic parts, *Advanced Engineering Materials* 21(6) (2019).
- [23] M. Makowska, S. Pfeiffer, N. Casati, K. Florio, M. Vetterli, K. Wegener, T. Graule, H. van Swygenhoven, Pre-processing of hematite-doped alumina granules for selective laser melting, *Ceramics International* 45(14) (2019) 17014-17022.
- [24] X. Zhang, S. Pfeiffer, P. Rutkowski, M. Makowska, D. Kata, J. Yang, T. Graule, Laser cladding of manganese oxide doped aluminum oxide granules on titanium alloy for biomedical applications, *Applied Surface Science* 520 (2020) 146304.
- [25] K. Florio, D. Puccio, G. Viganò, S. Pfeiffer, F. Verga, M. Grasso, B.M. Colosimo, T. Graule, K. Wegener, Process characterization and analysis of ceramic powder bed fusion, *The International Journal of Advanced Manufacturing Technology* (2021).
- [26] S. Pfeiffer, M. Makowska, F. Kevin, D.F. Sanchez, F. Marone, X. Zhang, C.G. Aneziris, H. Van Swygenhoven, K. Wegener, T. Graule, Selective laser melting of thermal pre-treated metal oxide doped aluminum oxide granules, *Open Ceramics* (2020) 100007.
- [27] S. Pfeiffer, K. Florio, M. Makowska, F. Marone, S. Yüzbasi, C.G. Aneziris, H. Van Swygenhoven, K. Wegener, T. Graule, Crack-reduced alumina/aluminum titanate composites additive manufactured by laser powder bed fusion of black TiO<sub>2</sub>-x doped alumina granules, *J. Eur. Ceram. Soc* 42(8) (2022) 3515-3529.
- [28] M. Mapar, D.Q. Zhang, Z.H. Liu, W.Y. Yeong, C.K. Chua, B.Y. Tay, O. Geramifard, S. Maleksaeedi, F.E. Wiria, Preparation and flowability characterization of ceramic powders for selective laser melting, *High value manufacturing: Advanced research in virtual and rapid prototyping*, Leira ,PT, 2014, pp. 267-271.
- [29] M. Mapar, Selective laser melting of ceramic-based materials for dental applications, Nanyang Technological University, 2014.

- [30] H. Liu, H. Su, Z. Shen, E. Wang, D. Zhao, M. Guo, J. Zhang, L. Liu, H. Fu, Direct formation of  $\text{Al}_2\text{O}_3/\text{GdAlO}_3/\text{ZrO}_2$  ternary eutectic ceramics by selective laser melting: Microstructure evolutions, *J. Eur. Ceram. Soc* 38(15) (2018) 5144-5152.
- [31] E. Strumza, P. Landau, G. Kimmel, Y.I. Ganor, O. Yeheskel, S. Hayun, Thermophysical properties of Ti-6Al-4V fabricated by powder bed fusion methods, *Additive Manufacturing* 58 (2022) 103045.
- [32] E. Strumza, O. Yeheskel, S. Hayun, The effect of texture on the anisotropy of thermophysical properties of additively manufactured  $\text{AlSi10Mg}$ , *Additive Manufacturing* 29 (2019) 100762.
- [33] K. Zhang, T. Liu, W. Liao, C. Zhang, Y. Yan, D. Du, Influence of laser parameters on the surface morphology of slurry-based  $\text{Al}_2\text{O}_3$  parts produced through selective laser melting, *Rapid Prototyping Journal* 24(2) (2018) 333-341.
- [34] J. Wilkes, Y.C. Hagedorn, W. Meiners, K. Wissenbach, Additive manufacturing of  $\text{ZrO}_2\text{-Al}_2\text{O}_3$  ceramic components by selective laser melting, *Rapid Prototyping Journal* (2013).
- [35] A.W. Sleight, Isotropic negative thermal expansion, *Annual review of materials science* 28(1) (1998) 29-43.
- [36] T. Mary, J. Evans, T. Vogt, A. Sleight, Negative thermal expansion from 0.3 to 1050 Kelvin in  $\text{ZrW}_2\text{O}_8$ , *Science* 272(5258) (1996) 90-92.
- [37] K. De Buysser, P. Lommens, C. De Meyer, E. Bruneel, S. Hoste, I. Van Driessche,  $\text{ZrO}_2\text{-ZrW}_2\text{O}_8$  composites with tailor-made thermal expansion, *Ceramics-Silikaty* 48(4) (2004) 139-144.
- [38] L.L.Y. CHANG, M.G. SCROGER, B. PHILLIPS, Condensed Phase Relations in the Systems  $\text{ZrO}_2\text{-WO}_2\text{-WO}_3$  and  $\text{HfO}_2\text{-WO}_2\text{-WO}_3$ , *Journal of the American Ceramic Society* 50(4) (1967) 211-215.
- [39] S. Jacob, J. Javornizky, G.H. Wolf, C.A. Angell, Oxide ion conducting glasses: synthetic strategies based on liquid state and solid state routes, *Int. J. Inorg. Chem* 3(3) (2001) 241-251.
- [40] V.A. Petrov, Abrupt increase of the absorption coefficient of alumina at melting by laser radiation and its decrease at solidification, *Int. J. Thermophys.* 30(6) (2009) 1938-1959.
- [41] L. Sun, P. Kwon,  $\text{ZrW}_2\text{O}_8/\text{ZrO}_2$  composites by in situ synthesis of  $\text{ZrO}_2\text{+WO}_3$ : Processing, coefficient of thermal expansion, and theoretical model prediction, *Materials Science and Engineering: A* 527(1-2) (2009) 93-97.
- [42] J.-C. Chen, G.-C. Huang, C. Hu, J.-P. Weng, Synthesis of negative-thermal-expansion  $\text{ZrW}_2\text{O}_8$  substrates, *Scripta Materialia* 49(3) (2003) 261-266.
- [43] C.P. Romao, B.A. Marinkovic, U. Werner-Zwanziger, M.A. White, Thermal Expansion Reduction in Alumina-Toughened Zirconia by Incorporation of Zirconium Tungstate and Aluminum Tungstate, *Journal of the American Ceramic Society* 98(9) (2015) 2858-2865.
- [44] C.Y. Ho, R.E. Taylor, Thermal expansion of solids, *ASM international* 1998.
- [45] K.K. Chawla, *Ceramic matrix composites*, Springer Science & Business Media 2013.
- [46] N.K. Sharma, R.K. Misra, S. Sharma, Modeling of thermal expansion behavior of densely packed  $\text{Al/SiC}$  composites, *Int. J. Solids Struct.* 102-103 (2016) 77-88.
- [47] C. Karch, *Micromechanical analysis of thermal expansion coefficients, Modeling and Numerical Simulation of Material Science* 2014 (2014).
- [48] D. de Faoite, D.J. Browne, F.R. Chang-Díaz, K.T. Stanton, A review of the processing, composition, and temperature-dependent mechanical and thermal properties of dielectric technical ceramics, *Journal of Materials Science* 47(10) (2012) 4211-4235.
- [49] Aluminum Oxide,  $\text{Al}_2\text{O}_3$  Ceramic Properties; <https://accuratus.com/alumox.html>. (Accessed 11.06.2021).
- [50] S. Bandi, D. Vidyasagar, S. Adil, M.K. Singh, J. Basu, A.K. Srivastav, Crystallite size induced bandgap tuning in  $\text{WO}_3$  derived from nanocrystalline tungsten, *Scripta Materialia* 176 (2020) 47-52.
- [51] A. Sinhamahapatra, J.-P. Jeon, J. Kang, B. Han, J.-S. Yu, Oxygen-Deficient Zirconia ( $\text{ZrO}_{2-x}$ ): A New Material for Solar Light Absorption, *Sci. Rep.* 6(1) (2016) 27218.
- [52] E. Liang, T. Wu, B. Yuan, M. Chao, W. Zhang, Synthesis, microstructure and phase control of zirconium tungstate with a  $\text{CO}_2$  laser, *Journal of Physics D: Applied Physics* 40(10) (2007) 3219.
- [53] H. Najafi-Ashtiani, A. Bahari, S. Gholipour, S. Hoseinzadeh, Structural, optical and electrical properties of  $\text{WO}_3\text{-Ag}$  nanocomposites for the electro-optical devices, *Appl. Phys. A* 124(1) (2017) 24.



- [54] C.M. PHILLIPPI, K.S. MAZDIYASNI, Infrared and Raman Spectra of Zirconia Polymorphs, *Journal of the American Ceramic Society* 54(5) (1971) 254-258.
- [55] J. Wu, H. Lin, J. Li, L. Long, J. Li, G. Guo, Structural Studies of WO<sub>3</sub>-Catalysed Mullite, *Adv. Eng. Mater.* 10(6) (2008) 588-591.
- [56] J. Sauter, Die Grössenbestimmung der im Gemischnebel von Verbrennungskraftmaschinen vorhandenen Brennstoffteilchen: (Mitteilung aus dem Laboratorium für Technische Physik der Technischen Hochschule München), VDI-Verlag 1926.
- [57] K.F. Young, H.P.R. Frederikse, Compilation of the Static Dielectric Constant of Inorganic Solids, *Journal of Physical and Chemical Reference Data* 2(2) (1973) 313-410.
- [58] K.M. Karuppasamy, A. Subrahmanyam, Results on the electrochromic and photocatalytic properties of vanadium doped tungsten oxide thin films prepared by reactive dc magnetron sputtering technique, *Journal of Physics D: Applied Physics* 41(3) (2008) 035302.
- [59] D.L. Wood, K. Nassau, Refractive index of cubic zirconia stabilized with yttria, *Applied Optics* 21(16) (1982) 2978-2981.
- [60] J.-P. Choi, G.-H. Shin, S. Yang, D.-Y. Yang, J.-S. Lee, M. Brochu, J.-H. Yu, Densification and microstructural investigation of Inconel 718 parts fabricated by selective laser melting, *Powder Technology* 310 (2017) 60-66.
- [61] R. Engeli, T. Etter, S. Hövel, K. Wegener, Processability of different IN738LC powder batches by selective laser melting, *Journal of Materials Processing Technology* 229 (2016) 484-491.
- [62] M. Vetterli, Powder optimization for laser sintering: An insight in powder intrinsic and extrinsic properties, ETH Zurich, Zurich, 2019.
- [63] P. Kubelka, F. Munk, Ein Beitrag zur Optik der Farbanstriche (Contribution to the optic of paint), *Zeitschrift für Technische Physik* 12 (1931) 593-601.
- [64] J.M. Olinger, P.R. Griffiths, Quantitative effects of an absorbing matrix on near-infrared diffuse reflectance spectra, *Analytical Chemistry* 60(21) (1988) 2427-2435.
- [65] K. Kendall, Adhesion: Molecules and Mechanics, *Science* 263(5154) (1994) 1720-1725.
- [66] F. Iskandar, L. Gradon, K. Okuyama, Control of the morphology of nanostructured particles prepared by the spray drying of a nanoparticle sol, *J. Colloid Interface Sci.* 265(2) (2003) 296-303.
- [67] S. Lichtenberg, Charakterisierung von Elektroden für Hochdruck-Plasmalampen durch elektrische Messungen und Modellierungen, Tenea Verlag Ltd. 2004.
- [68] D.A. Woodcock, P. Lightfoot, C. Ritter, Negative thermal expansion in Y<sub>2</sub>(WO<sub>4</sub>)<sub>3</sub>, *J. Solid State Chem.* 149(1) (2000) 92-98.
- [69] J. Evans, T. Mary, A. Sleight, Negative thermal expansion in a large molybdate and tungstate family, Elsevier, 1997, pp. 580-583.
- [70] N. Imanaka, M. Hiraiwa, G. Adachi, H. Dabkowska, A. Dabkowski, Thermal contraction behavior in Al<sub>2</sub>(WO<sub>4</sub>)<sub>3</sub> single crystal, *J. Cryst. Growth* 220(1-2) (2000) 176-179.
- [71] S. Achary, G. Mukherjee, A. Tyagi, S. Vaidya, Preparation, thermal expansion, high pressure and high temperature behavior of Al<sub>2</sub>(WO<sub>4</sub>)<sub>3</sub>, *J. Mater. Sci.* 37(12) (2002) 2501-2509.
- [72] L.P. Prisco, P.I. Pontón, M.V. Guamán, R.R. Avillez, C.P. Romao, M.B. Johnson, M.A. White, B.A. Marinkovic, Assessment of the thermal shock resistance figures of merit of Al<sub>2</sub>W<sub>3</sub>O<sub>12</sub>, a low thermal expansion ceramic, *Journal of the American Ceramic Society* 99(5) (2016) 1742-1748.
- [73] L.P. Prisco, M. Marzano, P.I. Pontón, A.M. Costa, C.A. da Costa Neto, G. Sweet, C.P. Romao, M.A. White, B.A. Marinkovic, Relationship between sintering methods and physical properties of the low positive thermal expansion material Al<sub>2</sub>W<sub>3</sub>O<sub>12</sub>, *Int. J. Appl. Ceram. Technol.* 16(1) (2019) 346-356.
- [74] P. Auerkari, Mechanical and physical properties of engineering alumina ceramics, 1996.
- [75] F.R. Drymiotis, H. Ledbetter, J.B. Betts, T. Kimura, J.C. Lashley, A. Migliori, A.P. Ramirez, G.R. Kowach, J. Van Duijn, Monocrystal Elastic Constants of the Negative-Thermal-Expansion Compound Zirconium Tungstate (ZrW<sub>2</sub>O<sub>8</sub>), *Phys. Rev. Lett.* 93(2) (2004) 025502.
- [76] E.Y. Fogaing, Y. Lorgouilloux, M. Huger, C.P. Gault, Young's modulus of zirconia at high temperature, *J. Mater. Sci.* 41(22) (2006) 7663-7666.
- [77] X. Liu, H.-Q. Fan, Electronic structure, elasticity, Debye temperature and anisotropy of cubic WO<sub>3</sub> from first-principles calculation, *R. Soc. Open Sci.* 5(6) (2018) 171921.

- [78] P. Jardim, E. Garcia, B. Marinkovic, Young's modulus, hardness and thermal expansion of sintered  $\text{Al}_2\text{W}_3\text{O}_{12}$  with different porosity fractions, *Ceramics International* 42(4) (2016) 5211-5217.

Journal Pre-proof



**Declaration of interests**

☒ The authors declare that they have no known competing financial interests or personal relationships that could have appeared to influence the work reported in this paper.

☐ The authors declare the following financial interests/personal relationships which may be considered as potential competing interests:

Journal Pre-proof